Available online at www.sciencedirect.com
ScienceDirect
International Journal of Heat and Fluid Flow 28 (2007) 72–82
International Journal of HEAT AND FLUID FLOW
www.elsevier.com/locate/ijhff

Numerical simulation of gas–liquid two-phase flow and convective heat transfer in a micro tube

Koji Fukagata [a,*], Nobuhide Kasagi [a], Poychat Ua-arayaporn [a], Takehiro Himeno [b]

[a] Department of Mechanical Engineering, The University of Tokyo, Hongo 7-3-1, Bunkyo-ku, Tokyo 113-8656, Japan
[b] Department of Aeronautics and Astronautics, The University of Tokyo, Hongo 7-3-1, Bunkyo-ku, Tokyo 113-8656, Japan

Accepted 27 April 2006
Available online 25 September 2006

Abstract

Numerical simulation of an air and water two-phase flow in a 20 μm ID tube is carried out. A focus is laid upon the flow and heat transfer characteristics in bubble-train flows. An axisymmetric two-dimensional flow is assumed. The finite difference method is used to solve the governing equations, while the level set method is adopted for capturing the interface of gas and liquid. In each simulation, the mean pressure gradient and the wall heat flux are kept constant. The simulation is repeated under different conditions of pressure gradient and void fraction. The superficial Reynolds numbers of gas and liquid phases studied are 0.34–13 and 16–490, respectively, and the capillary number is 0.0087–0.27. Regardless of the flow conditions, the gas-phase velocity is found approximately 1.2 times higher than the liquid-phase velocity. This is in accordance with the Armand correlation valid for two-phase flows in macro-sized tubes. The two-phase friction coefficient is found to be scaled with the Reynolds number based on the effective viscosity of the Einstein type. The computed wall temperature distribution is qualitatively similar to that observed experimentally in a mini channel. The local Nusselt number beneath the bubble is found notably higher than that of single-phase flow.

Keywords: Two-phase flow; Numerical simulation; Gas–liquid flow; Micro tube; Bubble; Pressure drop; Heat transfer

1. Introduction

Multiphase flow in a micro conduit has become very important in many emerging applications such as micro heat exchangers and Lab-on-a-chip. In order to successfully design such devices, understanding of flow physics in micro scale and their engineering modeling are crucial.

Gas–liquid two-phase flows in mini and micro conduits often exhibit different behavior as compared to those in macro-sized conduits. One reason for this difference is the ratio of the gravitational effects to the surface tension, which can be represented by the Eötvös number (or the Bond number):

$$Eo = \frac{g\Delta\rho d^2}{\sigma}, \tag{1}$$

where g, $\Delta\rho$, d and σ denote the gravitational acceleration, the density difference between two phases, the hydraulic diameter of conduit, and the surface tension. For instance, Brauner and Moalem-Maron (1992) propose a criterion, $Eo \ll (2\pi)^2$, for the surface tension to be dominant.

As reviewed, e.g., by Kandlikar (2002), Lee and Mudawar (2005b), and Serizawa (2006), extensive experimental studies have been reported on gas–liquid two-phase flow and boiling heat transfer in mini and micro conduits. The primary concerns lie in the pressure drop and heat transfer characteristics under given flow conditions. However, there still seem to exist considerable discrepancies between experimental data, especially in heat transfer characteristics, largely due to the difficulty in experimental setup and measurement.

* Corresponding author.
E-mail address: fukagata@thtlab.t.u-tokyo.ac.jp (K. Fukagata).

0142-727X/$ - see front matter © 2006 Elsevier Inc. All rights reserved.
doi:10.1016/j.ijheatfluidflow.2006.04.010

Nomenclature

A	cross-sectional area of tube, $A = \pi R^2$
C	Chisholm parameter
Ca	Capillary number, $\mu_L j_L/\sigma$
C_p	specific heat at constant pressure
d	hydraulic diameter
Eo	Eötvös number, Eq. (1)
f_{TP}	two-phase friction factor, Eq. (22)
F	level set function
g	gravitational acceleration
G	total mass flux, $\rho_L j_L + \rho_G j_G$
h	heat transfer coefficient
H_ε	smoothed Heaviside function, Eq. (7)
j	superficial velocity
L_z	longitudinal length of computational domain
$\vec{n}$	unit normal vector
Nu	Nusselt number, Eq. (36)
p	pressure
P	mean pressure
Q	volumetric flow rate
R	radius of tube
R_b	radius of bubble
Re	superficial Reynolds number, $\rho_k j_k (2R)/\mu_k$ (where $k = G, L$)
t	time
T	local temperature
u	local velocity
u_c	velocity magnitude of circulating flow
U	mean velocity, Eqs. (29) and (30)
X	Martinelli parameter, Eq. (19)
z	longitudinal coordinate

Greek Symbols

α	void fraction
β	volumetric gas flow ratio, Eq. (14)
δ	Dirac delta function
δ_ε	smoothed Dirac delta function, Eq. (8)
Δr	radial grid spacing
Δz	longitudinal grid spacing
$\Delta\rho$	density difference
ε	dimensionless width of interface smoothing
ϕ	any variable
Φ_L^2	two-phase multiplier, Eq. (18)
κ	interface curvature
λ	heat conductivity
μ	dynamic viscosity
ρ	density
σ	surface tension coefficient
θ	dimensionless local temperature, Eq. (34)
Θ	dimensionless mean temperature
Ψ	dimensionless stream function, Eq. (31)

Subscripts

a	actual
G	gas phase
GO	gas-only
H	homogeneous
L	liquid phase
LO	liquid-only
m	bulk-mean
r	radial
TP	two-phase
u	unknown
w	wall
z	longitudinal

Operator

$\langle \cdot \rangle$	domain average

Numerous visualization studies show that gas–liquid flows in micro sized conduits do not have a high degree of three-dimensionality. Therefore, their dynamics is expected much simpler than those in macro-sized conduits. By focusing on this reduced complexity, several attempts have recently been made to develop simple mechanistic models, rather than tuning the conventional models for micro conduits, e.g., a surface tension-conscious two-phase pressure drop model by Lee and Mudawar (2005a) and the three-zone boiling heat transfer model by Thome et al. (2004). Basically, these models largely rely on experimentally accessible information (such as flow patterns), dimensional analysis, and assumptions of velocity and temperature profiles. These mechanistic models can be much improved if we have more detailed knowledge inside the flow. With the present measurement technique, information inside a micro two-phase flow, such as the local velocity and temperature, is difficult (or perhaps impossible) to obtain. In contrast, advanced numerical simulation has a possibility to offer those quantities.

Our final goal is to perform systematic simulation of boiling heat transfer in micro conduit in order to obtain comprehensive understanding of two-phase flow physics and heat transport mechanisms in micro conduits. As the first step, we numerically investigate the essential mechanisms of isothermal bubble-train flow and convective heat transfer without phase change. The global properties obtained in the simulation are compared with available experimental data and empirical correlations. The underlying mechanisms are discussed based on the computed flow characteristics. Similar attempts have been made recently by Ghidersa et al. (2004), who simulated heat transfer in bubble-train flow in a three-dimensional square mini-channel. In the present study, we deal with two-dimensional axisymmetric bubble-train flows. Accordingly, analysis of flow and heat transfer characteristics is

much simplified, while retaining the essential physical features.

2. Simulation methods

2.1. Governing equations

We consider a gas–liquid two-phase flow in a cylindrical pipe. Each phase is treated as incompressible. The gas and liquid are immiscible and phase change does not take place. Under these assumptions, the fluid velocity field, $\vec{u}$, is given by the continuity equation:

$$\nabla \cdot \vec{u} = 0, \tag{2}$$

and the momentum equation,

$$\frac{\partial(\rho\vec{u})}{\partial t} + \vec{u}\cdot\nabla(\rho\vec{u}) = -\nabla p + \nabla\cdot\left[\mu\left(\nabla\vec{u} + (\nabla\vec{u})^t\right)\right] - \sigma\kappa\delta\vec{n}, \tag{3}$$

where ρ and μ denote the density and the dynamic viscosity, respectively. The last term of Eq. (3) represents the surface tension force, with κ, δ, and $\vec{n}$ denoting the curvature (viewed from the gas phase), the Dirac delta function, and the unit normal vector of the interface (outward from the gas to liquid phases), respectively. The gravitational force term is omitted because Eo is estimated to be on the order of 10^{-4} under the conditions assumed in the present study.

We also consider convective heat transfer. By assuming small temperature difference, the temperature is treated as a passive scalar. Thus, the governing equation for temperature, T, reads

$$\frac{\partial(\rho C_p T)}{\partial t} + \vec{u}\cdot\nabla(\rho C_p T) = \nabla\cdot(\lambda\nabla T), \tag{4}$$

where C_p and λ are the specific heat at constant pressure and the heat conductivity, respectively.

Note that Eqs. (2)–(4) are satisfied in both gas and liquid phases.

2.2. Interface capturing method

In order to accurately capture the gas–liquid interface, we adopt the level set method (Sussman et al., 1994). The interface is captured implicitly as the zero level set of a smooth function, which is denoted as F; the gas–liquid interface is identified as $F = 0$. The level set function is negative in the gas ($F < 0$) and positive in the liquid ($F > 0$). The function of F follows the advection equation:

$$\frac{\partial F}{\partial t} + \vec{u}\cdot\nabla F = 0. \tag{5}$$

The physical properties of the fluid are calculated by interpolating those of the gas and liquid phases, according to

$$\phi = \left(\frac{1}{2} + H_\varepsilon\right)\phi_{\mathrm{L}} + \left(\frac{1}{2} - H_\varepsilon\right)\phi_{\mathrm{G}}. \tag{6}$$

Here, ϕ denotes any physical property (ρ, μ, C_p, and λ) with its subscripts, L and G, representing the liquid and gas, respectively. The interpolation function H_ϵ is a smoothed Heaviside function defined as

$$H_\varepsilon(F) = \begin{cases} -\frac{1}{2} & \text{for } F \leqslant -\varepsilon \\ \frac{1}{2}\left[\left(\frac{F}{\varepsilon}\right) + \frac{1}{\pi}\sin\left(\frac{\pi F}{\varepsilon}\right)\right] & -\varepsilon < F < \epsilon \\ \frac{1}{2} & F \geqslant \varepsilon, \end{cases} \tag{7}$$

where ε is the width of interface smoothing. In the present simulation, ε is set equal to the length of three computational grid cells.

The surface tension term in Eq. (3) is computed by using the continuum surface force model (Brackbill et al., 1992). The Dirac delta function in the surface tension term is replaced by a smoothed Dirac delta function, δ_ε, which is defined as

$$\delta_\varepsilon(F) = \frac{\mathrm{d}H_\varepsilon}{\mathrm{d}F} = \begin{cases} \frac{1}{2}\left[\frac{1}{\varepsilon} + \frac{1}{\varepsilon}\cos\left(\frac{\pi F}{\varepsilon}\right)\right] & \text{for } |F| < \varepsilon \\ 0 & |F| \geqslant \varepsilon. \end{cases} \tag{8}$$

The curvature of the interface is calculated by

$$\kappa = \nabla\cdot\vec{n}, \tag{9}$$

where the unit vector normal to the interface is computed from the level set function, i.e.,

$$\vec{n} = \frac{\nabla F}{|\nabla F|}. \tag{10}$$

2.3. Flow and boundary conditions

In the present study, only the bubble-train flow is considered. Thus, the flow is assumed axisymmetric, so a two-dimensional $(r - z)$ computational domain is employed. The periodic boundary condition is applied at the both ends and no-slip condition is applied at the wall. Four different lengths of computational domain, i.e., $L_z/R = 2$, 3, 4 and 8, are examined.

For the temperature field, a uniform wall heat flux is assumed. A quasi-periodic boundary condition,

$$\left.\frac{\partial T}{\partial z}\right|_{z=0} = \left.\frac{\partial T}{\partial z}\right|_{z=L_z} \tag{11}$$

is applied on the both ends. Note that, strictly speaking, this formulation is ill-posed, because all the boundary conditions are of the Neumann type. The temperature field computed with this formulation contains an unknown temperature T_{u} in addition to the actual temperature T_{a}, viz.,

$$T(r,z,t) = T_{\mathrm{a}}(r,z,t) + T_{\mathrm{u}}(t). \tag{12}$$

In order to obtain the actual temperature, the value of T_{u} should be computed from the global energy balance. In the present study, however, this procedure is omitted because the temperature is treated as a passive scalar and only the temperature difference is of interest.

2.4. Discretization procedure

The governing equations are solved under the above-mentioned boundary conditions by using the SMAC method (Amsden and Harlow, 1970). The second-order accurate central difference scheme is used for the spatial discretization. The pressure Poisson equation is solved by using the successive over-relaxation (SOR) scheme. An equally spaced staggered grid system is adopted. The grid is uniform both in the longitudinal (z) and radial (r) directions. The grid size is fixed at $\Delta r/R = \Delta z/R = 0.03125$, and this corresponds to 32 grid cells in the radial direction. It has been numerically verified that this grid resolution is sufficient (Ua-arayaporn, 2005).

Integration of the advection Eq. (5) is done by the CIP scheme (Yabe et al., 1991), which is compact, bounded and of nearly spectral accuracy (Yabe et al., 2001). The level-set function, F, is designed as a distance function, which measures the distance from the bubble surface. However, this nature is not simply conserved by Eq. (5). Maintaining F as a distance function is essential for providing the correct interface force and the fixed interface thickness. Thus, the re-initialization procedure (Sussman et al., 1994) with mass conservation constraint (Sussman and Fatemi, 1999) is made at every computational time step. In addition, a global mass correction procedure is applied in order to ensure the mass conservation for entire computation time. Other details of the CIP level-set method used here are similar to those used in Himeno et al. (2005).

The CIP scheme is also used here for the advection term of the energy Eq. (4) in order to capture a steep temperature gradient expected near the gas–liquid interface.

3. Results and discussion

We assume water and air at 25 °C (298 K) and 1 atm ($\rho_L = 1.0\times10^3$ kg/m^3, $\mu_L = 8.9\times10^{-4}$ Pa s; $\rho_G = 1.2$ kg/m^3, $\mu_G = 1.8\times10^{-5}$ Pa s; $\sigma = 7.2\times10^{-2}$ N/m) and the radius R of the cylindrical tube is fixed at 10 μm. The condition is similar to that in the experiment by Serizawa et al. (2002). The simulation is performed for different values of void fraction, α, and pressure gradient, $-dP/dz$. Each simulation is started with gas and liquid at rest. One bubble is initially placed in the computational domain. The pressure gradient is kept constant and the simulation is continued until the flow becomes fully developed. Ten cases were simulated with $-dP/dz = 8.5\times10^1 - 3.0\times10^3$ MPa/m and $\alpha = 0.2 - 0.6$. The given and resultant major flow parameters are summarized in Table 1. It should be stressed again that, unlike the experiment by Serizawa et al. (2002), the present simulation is run under a given void fraction and pressure gradient (bold letters in Table 1), and the flow rate that satisfies this condition is the solution. The resultant flow parameters (plain letters in Table 1) are calculated by using this solution, but not given ones.

Fig. 1 shows the computed superficial gas and liquid velocities, j_G and j_L, which are defined as

Table 1
Given (bold) and resultant flow parameters

Case	**Void fraction α**	**Pressure gradient $(-dP/dz)_{TP}$ [MPa/m]**	**Bubble period L_z/R**	Superficial liquid velocity j_L [m/s]	Superficial gas velocity j_G [m/s]	Superficial liquid Reynolds number Re_L	Superficial gas Reynolds number Re_G	Capillary number Ca_L	Martinelli parameter X	Two-phase multiplier Φ_L^2	Volumetric gas flow ratio β
A	**0.20**	**85**	**4**	0.71	0.26	16	0.34	0.0087	11.5	1.69	0.27
B	**0.20**	**570**	**4**	4.3	1.5	97	1.9	0.053	11.9	1.85	0.26
C	**0.20**	**850**	**2**	6.3	2.6	140	3.4	0.078	10.8	1.90	0.30
D	**0.20**	**850**	**3**	6.4	2.3	140	3.0	0.078	11.5	1.88	0.27
E	**0.20**	**850**	**4**	6.3	2.2	140	2.9	0.078	11.7	1.90	0.26
F	**0.20**	**850**	**8**	7.0	2.7	160	3.5	0.086	11.3	1.72	0.28
G	**0.20**	**3000**	**4**	22	9.9	490	13	0.27	10.3	1.95	0.31
H	**0.30**	**750**	**4**	4.3	2.8	95	3.6	0.053	8.71	2.46	0.39
I	**0.42**	**620**	**4**	2.8	3.2	62	4.1	0.034	6.54	3.12	0.53
J	**0.60**	**430**	**4**	1.2	3.1	28	4.0	0.015	4.41	4.84	0.72

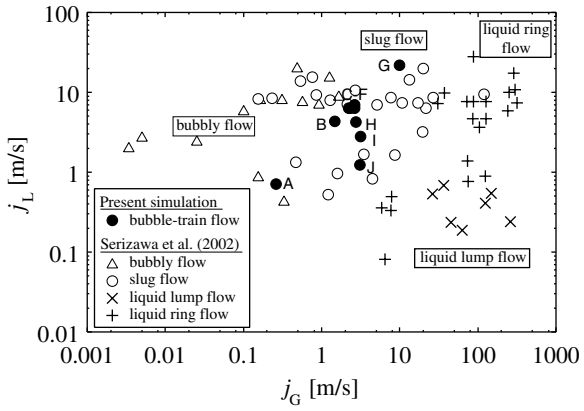

Fig. 1. Superficial velocities of air–water flow in 20 μm ID tube. Keys from A to J denote Cases in Table 1.

$$j_G = \frac{Q_G}{A}, \quad j_L = \frac{Q_L}{A}, \tag{13}$$

where Q_G and Q_L are the volumetric flow rates of the gas and liquid, respectively, and A is the cross-sectional area of the pipe. In all computed cases, the superficial velocities lie in the range of slug flow regime found by the experiment of Serizawa et al. (2002). The resultant superficial Reynolds numbers of the gas and liquid phases are $Re_G = \rho_G j_G(2R)/\mu_G = 0.34 - 13$ and $Re_L = \rho_L j_L(2R)/\mu_L = 16 - 490$, respectively. The capillary number is $Ca = \mu_L j_L/\sigma = 0.0087 - 0.27$.

3.1. Gas flow ratio

Fig. 2 shows the computed relation between the void fraction α and the gas volumetric flow ratio β defined as

$$\beta = \frac{Q_G}{Q_G + Q_L} = \frac{j_G}{j_G + j_L} = \alpha \frac{U_G}{U_{TP}}. \tag{14}$$

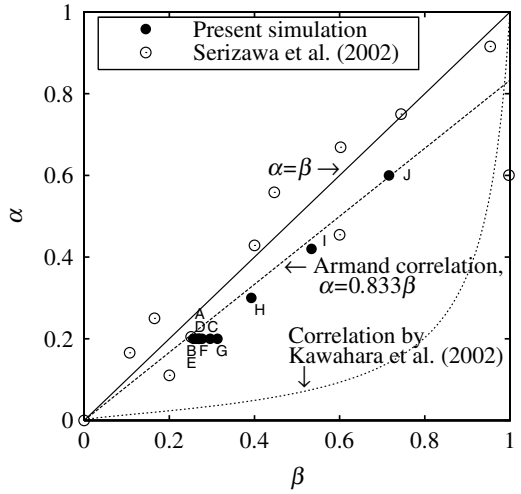

Fig. 2. Relationship between volumetric gas flow ratio (β) and void fraction (α).

Present results for $\alpha = 0.2$ are obtained with different pressure gradients and different sizes of computational box. The relation between α and β computed is found in good accordance with the Armand correlation (Armand and Treschev, 1946) proposed for conventional tubes, which reads:

$$\alpha = 0.833\beta. \tag{15}$$

The results are also compared with experimental data of bubbly and slug flows in Serizawa et al. (2002), the theoretical relationship for the homogeneous flow,

$$\alpha = \beta, \tag{16}$$

and the correlation proposed by Kawahara et al. (2002),

$$\alpha = \frac{0.03\beta^{0.5}}{1 - 0.97\beta^{0.5}}. \tag{17}$$

The correlation of Eq. (17) is based on the experimental data for a 100 μm ID tube at the superficial velocities comparable to the present conditions. The present results are in fair accordance with the experimental data by Serizawa et al. (2002), although most of their data seem to be distributed around the line of $\alpha = \beta$ rather than $\alpha = 0.833\beta$. The correlation by Kawahara et al. (2002) predicts much larger values of β. This may be due to the difference in flow patterns; the flows in Kawahara et al. (2002) experiment have a gas core causing much higher slip velocity. The most recent experiment by Kawahara et al. (2006) show that at the same flow conditions either quasi-separated flow (corresponding to Eq. (17)) or quasi-homogeneous flow ($\alpha \simeq \beta$) appears depending on differences of mixing condition at the inlet.

The small discrepancy between the present simulation results and the experimental data by Serizawa et al. (2002) can be explained as follows, at least for the case of relatively high void fraction ($0.4 < \alpha < 0.6$). As is noted by Serizawa et al. (2002), a dry zone may have been developed under the gas slug in their experiment. Therefore, the

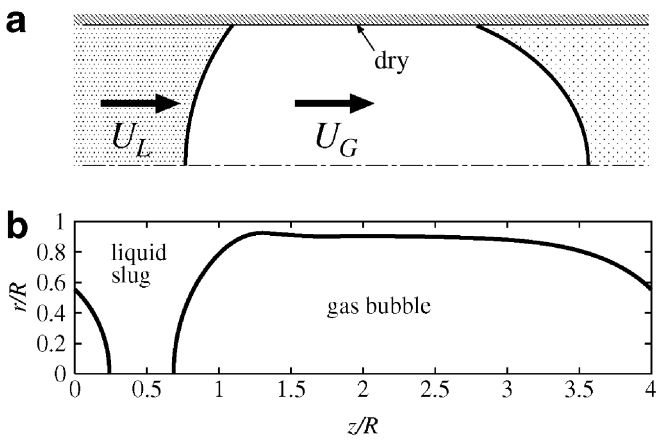

Fig. 3. Bubble shape in slug flow regime. (a) Probable shape in previous experiments (dry wall) and (b) present simulation with $\alpha = 0.6$, $-dP/dz = 430$ MPa/m (wet wall).

gas, liquid and two-phase velocities become all equal, as schematically shown in Fig. 3(a). Hence, $\beta/\alpha = U_G/U_{TP} = 1$. In the present simulation, in contrast, the wall is always wet as exemplified in Fig. 3(b). The possible reason for this difference may be the lack of special treatment for the three-phase (i.e., gas–liquid–solid) interface, of which scale is smaller than the numerical resolution. Such interface cannot be simply described by the macroscopic equations. In the present simulation, the liquid film between the bubble and wall (which is resolved by about six radial grid cells) has always a lower velocity than the gas velocity due to the no-slip wall, and this results in U_{TP} smaller than U_G (i.e., $\beta > \alpha$).

3.2. Frictional pressure loss

The frictional pressure loss is compared with the Lockhart–Martinelli model (Lockhart and Martinelli, 1949). Namely, the two-phase pressure gradient, $(-dP/dz)_{TP}$ (which in the present study is identical to the given pressure gradient, $-dP/dz$) is evaluated through the two-phase multiplier, Φ_L^2, and the Martinelli parameter, X, defined respectively as

$$\Phi_L^2 = \frac{(-dP/dz)_{TP}}{(-dP/dz)_{LO}}, \tag{18}$$

and

$$X^2 = \frac{(-dP/dz)_{LO}}{(-dP/dz)_{GO}}. \tag{19}$$

Here, $(-dP/dz)_{LO}$ and $(-dP/dz)_{GO}$ represent the pressure gradients required to drive single-phase liquid and gas flows at the same superficial velocities, respectively. For macro-sized tube, the relation between Φ_L^2 and X is usually given by the Chisholm (1967) correlation, which reads

$$\Phi_L^2 = 1 + \frac{C}{X} + \frac{1}{X^2}, \tag{20}$$

where C is the Chisholm parameter, of which value ranges between 5 and 20; $C = 5$ corresponds to cases where both phases are laminar, and $C = 20$ to cases where both phases are turbulent. Mishima and Hibiki (1996) suggested a modified expression by correlating their experimental data of air–water flow in mini-tubes of 1–4 mm in inner diameter. The Chisholm parameter in Mishima–Hibiki model is diameter-dependent and can be expressed as

$$C = 21[1 - \exp(-0.319d)], \tag{21}$$

where the inner diameter, d, is given in millimeter. In the present case of $d = 0.02$, Eq. (21) gives $C = 0.13$.

Fig. 4 shows the relationship between Φ_L^2 and X in the present simulation. Four curves of Chisholm correlation with $C = 20$, $C = 12$ (corresponding to cases of laminar liquid flow and turbulent gas flow), $C = 5$, and $C = 0.13$ (from Eq. (21)) are also drawn. Most of the present data with $\alpha = 2$ are found between the curves of $C = 5$ and $C = 12$ For higher void fraction (Cases H–J), Φ_L^2 is even higher than the curve of $C = 12$. This trend is opposite to that observed in many of the previous pressure drop measurements in micro and mini ($R \sim 100$–1000 μm) conduit, in which Φ_L^2 tends to be below the curve of $C = 5$. Similarly to the argument made for Fig. 3, the discrepancy may also be due to different flow patterns. Unfortunately, direct comparison with experiment by Serizawa et al. (2002) cannot be made because the pressure drop was not studied in their experiment.

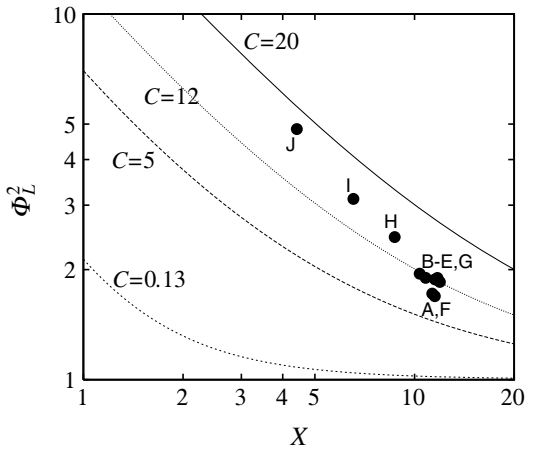

Fig. 4. Lockhart–Martinelli correlation. Solid circles denote the present data.

The pressure drop is also compared with homogeneous flow models. Fig. 5 shows the friction factor, f_{TP}, defined as

$$f_{TP} = \frac{4R(-dP/dz)_{TP}}{GU_{TP}}, \tag{22}$$

(where $G = \rho_L j_L + \rho_G j_G$ is the total mass flux), as functions of Reynolds number,

$$Re_H = \frac{2RG}{\mu_H}. \tag{23}$$

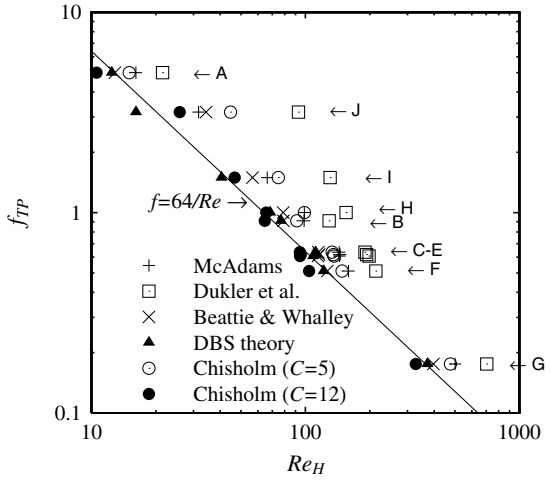

Fig. 5. Friction factor versus Reynolds numbers with different models of effective viscosity.

Different models have been proposed for the effective viscosity, μ_H. Here we examine the following four models.

- McAdams (1954):

$$\frac{1}{\mu_H} = \left(\frac{x}{\mu_G} + \frac{1-x}{\mu_L}\right), \tag{24}$$

- Dukker et al. (1964):

$$\mu_H = \beta\mu_G + (1-\beta)\mu_L, \tag{25}$$

- Beatie and Whalley (1982):

$$\mu_H = \beta\mu_G + (1-\beta)(1+2.5\beta)\mu_L, \tag{26}$$

- Theoretical solution for dilute bubble suspension (see, e.g., Wallis (1969)), denoted as DBS theory in Fig. 5:

$$\mu_H = (1+\beta)\mu_L. \tag{27}$$

The relationships using the effective viscosity corresponding to the Chisholm correlation, i.e.,

$$\mu_H = \frac{j_L}{U_{TP}}\left(1 + \frac{C}{X} + \frac{1}{X^2}\right)\mu_L, \tag{28}$$

are also shown for comparison. As shown in Fig. 5, all the empirical models introduced above seem to more or less overestimate the effective Reynolds number, viz., underestimate the effective viscosity. Although not shown here, the viscosity models by Owens (1961), Cicchitti et al. (1960) and Lin et al. (1991) were also examined. The results with these models were essentially similar to that with McAdams (1954). Surprisingly, the theoretical viscosity for dilute bubble suspension, Eq. (27), well reproduces the present results. Note that Eq. (27) corresponds to the well-known Einstein viscosity for solid particle suspension, $\mu_H = (1+2.5\beta)\mu_L$ (Einstein, 1906), but for bubbles. In order to explain this agreement, however, advanced theoretical investigation needs to be made in the future, because the bubble shape (not only spherical but also highly elongated) and flow condition ($\beta > 0.2$) in the present cases are totally different from those assumed in the derivation of Eq. (27) (i.e., spherical bubble with $\beta \ll 1$).

3.3. Velocity field

Fig. 6 shows the mean gas phase velocity, U_G, the mean liquid velocity, U_L, and the mean two-phase velocity, U_{TP}, computed under different pressure gradients at $\alpha = 0.2$. These velocities are defined, respectively, as

$$U_G = \frac{Q_G}{\alpha A} = \frac{j_G}{\alpha}, \quad U_L = \frac{Q_L}{(1-\alpha)A} = \frac{j_L}{1-\alpha}, \tag{29}$$

and

$$U_{TP} = \frac{Q_G + Q_L}{A} = j_G + j_L. \tag{30}$$

With the increase of pressure gradient, all three velocities increase almost linearly. The ratio of U_G to U_{TP} is slightly higher for a larger pressure gradient. The reason for this is

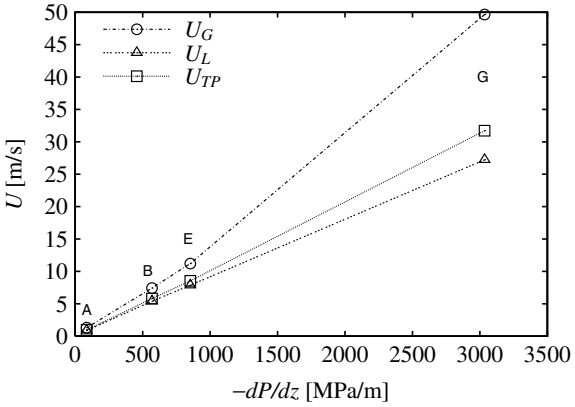

Fig. 6. Bulk mean velocities of gas phase (U_G) and liquid phase (U_L), and two-phase velocity (U_{TP}) under different pressure gradient ($\alpha = 0.2$, $R = 10$ μm).

indicated by the change of bubble shapes as shown in Fig. 7. With the increase of pressure gradient, the bubble is elongated in the central region of pipe and less influenced by the no-slip wall. Thus, the velocity ratio increases.

Also shown in Fig. 7 are the isolines of the dimensionless stream function relative to the bubble velocity, Ψ, defined as

$$\frac{u_r}{U_{TP}} = -\frac{R^2}{r}\frac{\partial\Psi}{\partial z}, \quad \frac{u_z - U_G}{U_{TP}} = \frac{R^2}{r}\frac{\partial\Psi}{\partial r}. \tag{31}$$

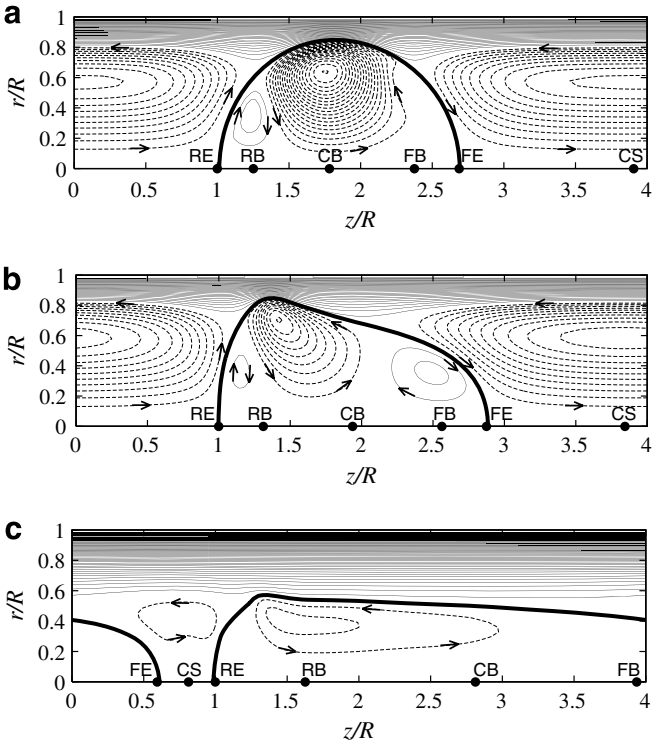

Fig. 7. Bubble shape (bold line) and relative streamlines when the rear end of bubble passes $z/R \simeq 1$ ($R = 10$ μm, $\alpha = 0.2$). Solid line, $\Psi < 0$ (clockwise circulation); dashed line, $\Psi > 0$ (anti-clockwise circulation); increment, 0.005. (a) $-dP/dz = 85$ MPa/m (Case A); (b) 850 MPa/m (Case E); (c) 3000 MPa/m (Case G). Solid circles on the cylindrical axis and corresponding keys denote the longitudinal positions in Fig. 8.

In Fig. 7a (Case A), an anti-clockwise circulation is found inside the bubble. The circulation is strong in the region close to the wall, where the gas–liquid interface is driven backward due to the strong shear. Accompanied with this, a clockwise circulation is also found in the rear part of the bubble. A circulation can also be found in the liquid region, in accordance with the sketch of possible streamlines given by Taylor (1961), and it results in continuous refreshment of the liquid layer near the wall and enhances the momentum transfer to the wall. Namely, the pressure drop increases due to this circulation. A similar circulation pattern has been shown experimentally (e.g., Thulasidas et al., 1997) and numerically (e.g., Irandoust and Andersson, 1989). With the increase in pressure gradient, the bubble becomes longer as shown in Fig. 7(b) (Case E) and Fig. 7(c) (Case G). In the case of intermediate pressure gradient (Case E), strong circulation is found also around the head of the bubble. It is clockwise and corresponds to the localized elongation of bubble.

Fig. 8 shows the radial distribution of the longitudinal (u_z) and radial (u_r) velocities in the cases presented in Fig. 7. Different longitudinal positions are defined:

- Rear end of bubble (RE),
- Rear part of bubble (RB),
- Central part of bubble (CB),
- Front part of bubble (FB),
- Front end of bubble (FE),
- Central part of liquid slug (CS).

The exact positions indicated by the keys, RE, RB, etc., are shown in Fig. 7. In Case A, where the bubble is nearly spherical, the profiles of u_z and u_r at FE are, respectively, nearly the same and nearly opposite to those at RE. This suggests that the velocity field in the liquid slug is nearly symmetric around the bubble. Inside the bubble, the velocity field is asymmetric as can be noticed from the profiles at FB and RB. At CS, the profile nearly coincides the laminar solution at the velocity of U_{TP}. In Case E, evolution of profiles inside the bubble is totally different from that in Case A, whilst the profile at CS remains nearly parabolic. The profile at CB is flattened like that of a turbulent flow due to stronger and complicated circulations, as observed in Fig. 7(b). Note that u_r/U_{TP} is nearly the same for Cases A and E, but the absolute radial velocity (u_r) in Case E is about nine times higher than that in Case A due to the difference of U_{TP}. Finally, in Case G, the relative variation of velocity inside the bubble is suppressed as compared to the former two cases.

In all the cases examined here, there are large variations of longitudinal and radial velocities in the liquid slug, which amount to 70% and 20% of U_{TP}, respectively. The velocity magnitude of circulating flow, u_c, may roughly be estimated as a product of a representative bubble radius, R_b, and the velocity gradient, i.e.,

$$u_c \sim R_b \left|\frac{\partial u_z}{\partial r}\right| \sim R_b \frac{U_{TP}}{R}. \tag{32}$$

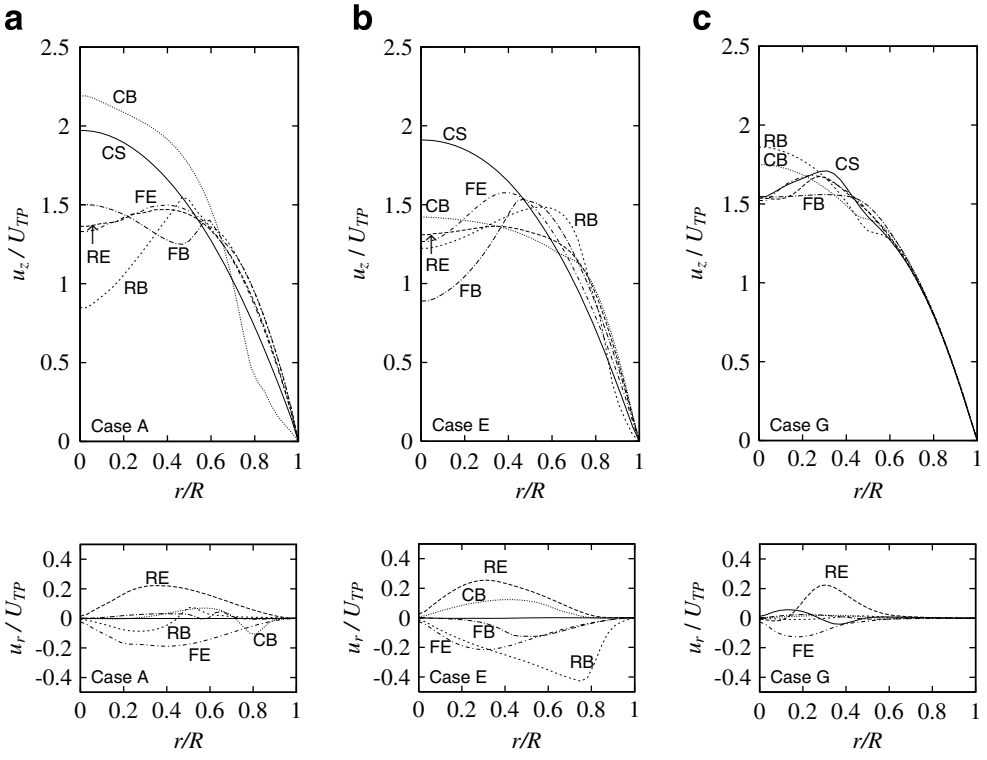

Fig. 8. Longitudinal (u_z) and radial (u_r) velocity profiles at different longitudinal positions. (a) Case A; (b) Case E; (c) Case G. See, Fig. 7 for positions indicated by keys.

Hence,

$$\frac{u_c}{U_{TP}} \sim \frac{R_b}{R}. \tag{33}$$

Usually, $R_b/R \ll 1$ in a macro-sized tube. In a micro sized tube, however, R_b is of comparable order to R. Thus, the circulating flow can become significantly strong. The momentum transfer due to the secondary flow is therefore considered to play a significant role in the determination of friction drag of bubble-train flow in a micro sized conduit.

In the discussion above, we mainly focused on the cases of single bubble period, i.e., $L_z/R = 4$. In two-phase flows, however, there may exist different flow patterns under a given set of flow conditions. In fact, recent experiment by Amador et al. (2004) shows that a nozzle of different diameters used for gas inlet results in different bubble periods under the same superficial velocities. Fig. 9 shows the bubble shape and the relative streamlines for the case of $\alpha = 0.2$ and $-dP/dz = 850$ MPa/m, but with different bubble periods (different computational box size), i.e., $L_z/R = 2$, 3 and 8. As the bubble period increases, the bubble is more elongated and the circulation pattern is also modified. Accordingly, the resultant flow parameters are slightly changed. As shown in Table 1, however, the amount of change is small.

3.4. Convective heat transfer

Fig. 10 shows the temperature contours at $\alpha = 0.2$ under different pressure gradients. Under the smaller pressure gradient (Fig. 10(a)), where the bubble shape is kept nearly spherical, the temperature contours inside the liquid slug align nearly parallel to the wall. Effects of convection due to the anti-clockwise circulation shown in Fig. 7(a) are noticed around the front and rear ends of the bubble. The situation is basically similar under the larger pressure gradient (Fig. 10(b)), although the temperature in the liquid slug is more homogenized due to the stronger circulation. In both cases, the temperature in the bubble is closer to the wall temperature and more homogeneous due to about 20 times higher thermal diffusivity than that of the liquid.

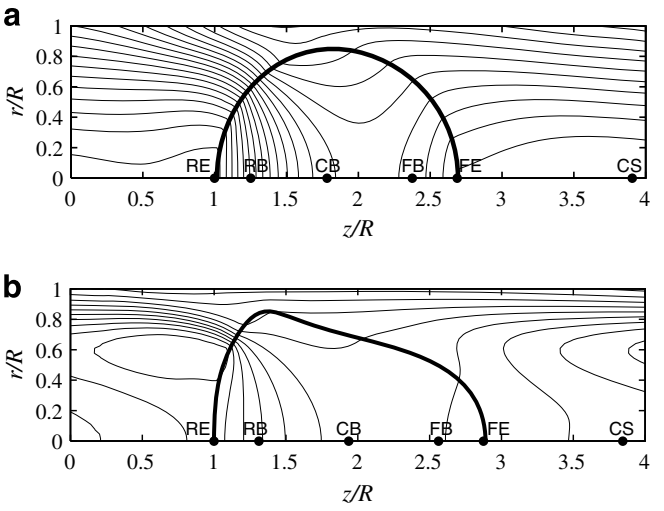

Fig. 10. Contour of dimensionless temperature (Eq. (34)) at $\alpha = 0.2$ in $R = 10$ μm tube. (a) $-dP/dz = 85$ MPa/m (Case A); (b) 850 MPa/m (Case E). Increment is 0.2.

Fig. 11 shows the streamwise distribution of the wall and bulk mean temperatures in the corresponding cases. The temperature is made dimensionless by using the domain-averaged wall and bulk mean temperatures, $\langle T_w \rangle$ and $\langle T_m \rangle$, as

$$\theta(r,z,t) = \frac{T(r,z,t) - \langle T_w \rangle}{\langle T_w \rangle - \langle T_m \rangle}, \tag{34}$$

(where the bracket, $\langle \cdot \rangle$, denotes the average in the longitudinal direction), and the dimensionless local bulk mean temperature is defined as

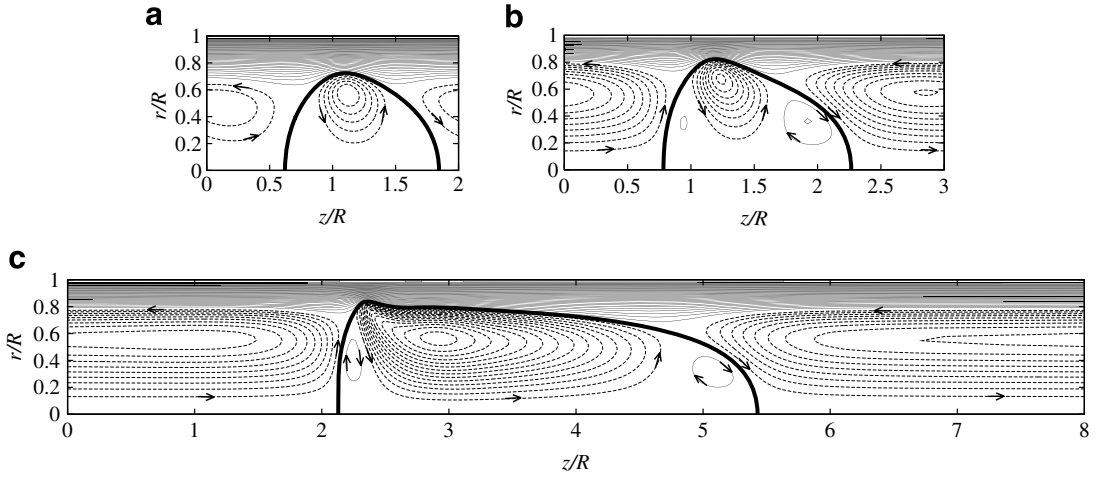

Fig. 9. Bubble shape (bold line) and relative streamlines for different bubble period ($R = 10$ μm, $\alpha = 0.2$, $-dP/dz = 850$ MPa/m). Solid line, $\Psi < 0$ (clockwise circulation); dashed line, $\Psi > 0$ (anti-clockwise circulation); increment, 0.005. (a) $L_z/R = 2$ (Case C); (b) $L_z/R = 3$ (Case D); (c) $L_z/R = 8$ (Case F).

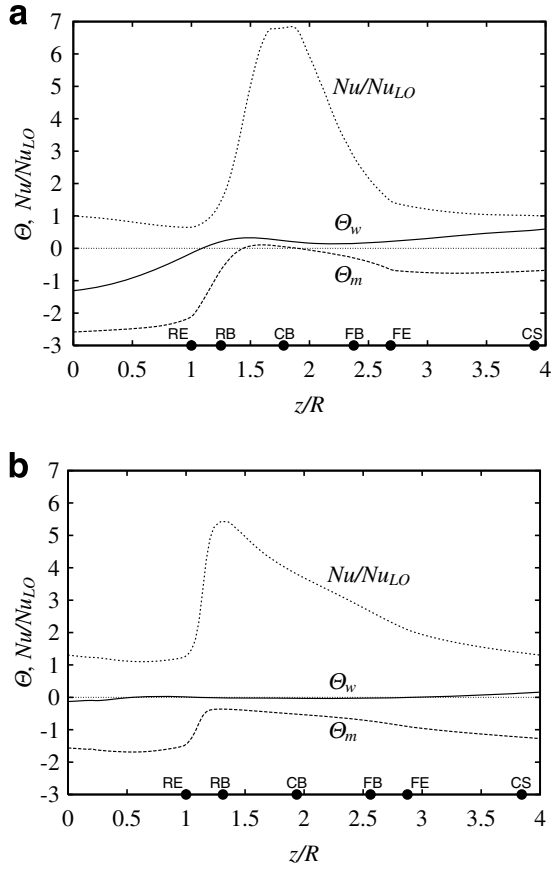

Fig. 11. Dimensionless local wall temperature (Θ_w), local bulk-mean temperature (Θ_m), and normalized local Nusselt number (Nu/Nu_{LO}). (a) Case A; (b) Case E.

$$\Theta_m(z,t) = \frac{\int_0^R \rho C_p u_z \theta r \mathrm{d}r}{\int_0^R \rho C_p u_z r \mathrm{d}r}. \tag{35}$$

In both cases shown in Fig. 11, the wall temperature locally peaks at the position where the tip of the bubble just passes. This observation qualitatively agrees with the experiment by Monde and Mitsutake (1995), who measured the wall temperature fluctuations at different streamwise positions in mini channels. Beneath the bubble, the bulk mean temperature is close to the wall temperature. The overall temperature change is milder in the case with a higher pressure gradient (Fig. 11(b)). This is attributed to more active renewal of thermal layer due to the stronger circulation in the liquid slug, as discussed above.

In Fig. 11, the local Nusselt number (normalized by the single-phase Nusselt number, $Nu_{LO} = 48/11 \simeq 4.36$) is shown. The local Nusselt number, $Nu(z,t)$, is defined as

$$Nu(z,t) = \frac{2Rh(z,t)}{\lambda_L} = \frac{2R(\partial\theta/\partial r)_w}{\Theta_w(z,t) - \Theta_m(z,t)}. \tag{36}$$

Because the wall heat flux is constant and the pipe wall is always wet in the present simulation, Nu, is simply proportional to the inverse of difference between the local wall and bulk mean temperatures. In the region of liquid slug, Nu/Nu_{LO} is close to unity. The slightly higher value than that in Fig. 11(b) is, again, due to mixing enhancement by the circulation. In the region where the bubble exists, Nu rises up to 5–7 times Nu_{LO} due to the small difference between Θ_w and Θ_m. Accordingly, the global Nusselt number, Nu_{TP}, defined as

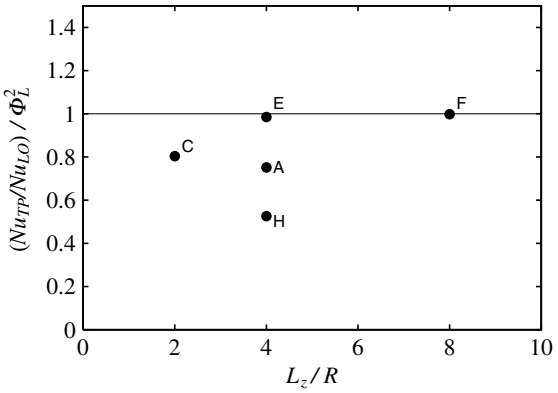

Fig. 12. Heat transfer enhancement at the expense of pumping power, $(Nu_{TP}/Nu_{LO})/\Phi_L^2$.

$$Nu_{TP} = \frac{2R(\partial\theta/\partial r)_w}{\langle\Theta_w\rangle - \langle\Theta_m\rangle}, \tag{37}$$

becomes also higher than Nu_{LO}; $Nu_{TP} = 5.55$ and 8.15 for the cases of Fig. 11(a) and (b), respectively.

The larger Nusselt number does not simply mean that the heat transfer performance is also better. For fair comparison, increase of pressure drop due to the introduction of bubbles should be taken into account. Fig. 12 shows the heat transfer enhancement at the expense of pumping power, $(Nu_{TP}/Nu_{LO})/\Phi_L^2$. As found from the figure, the factor does not exceed unity in the cases presently examined. Especially, the heat transfer performance is found worse than the single phase flow in the cases of weak pressure gradient (Case A), shorter bubble period (Case C), and high void fraction (Case H).

4. Conclusions

A series of numerical simulation are performed of air–water two-phase flows in a micro tube of 10 μm in radius. The flow conditions are set similar to those of the experiments by Serizawa et al. (2002).

The volumetric gas flow ratio computed in the present simulation are in good agreement with the correlations proposed for macro-sized flow. It is argued that the difference of wall condition above the bubble, i.e., whether the wall is kept wet or dry, explains small discrepancy with the experimental data. The frictional pressure drop is found higher than that predicted by the Chisholm correlation for laminar–laminar case. Investigation of flow pattern and velocity profiles reveals that strong circulations due to the presence of bubble play important role to enhance the momentum exchange in the radial direction.

The local Nusselt number is very large beneath the bubble due to small difference between wall and bulk mean temperatures. Heat transfer is also enhanced in the liquid slug due to the circulating flow. The global Nusselt number is higher than that in a single-phase flow. However, this increase occurs at the expense of pumping power.

It is also found that the length of the computational domain, i.e., the period of bubbles, considerably affects the flow pattern. This suggests that one must carefully design both numerical and experimental conditions in order to quantitatively compare them. The solution to this problem is left as a future work.

Acknowledgements

The authors are grateful to Drs. Y. Suzuki, N. Shikazono, and Y. Hasegawa (The University of Tokyo) for fruitful discussions and comments. This work was supported in part through the 21st Century COE Program, "Mechanical Systems Innovation", and in part through the Grant-in-Aid for Young Researcher (B) (No. 16760119) by the Ministry of Education, Culture, Sports, Science and Technology of Japan (MEXT).

References

Amador, C., Salman, W., Sanguanpiyapan, S., Gavriilidis, A., Angeli, P., 2004. Effect of gas/liquid inlet conditions on the mechanism of Taylor flow formation. In: Proc. 5th Int. Conf. Multiphase Flow, Paper 515.

Amsden, A.A., Harlow, F.H., 1970. The SMAC method: A numerical technique for calculating incompressible fluid flows. Los Alamos Report, LA-4370.

Armand, A.A., Treschev, G.G., 1946. The resistance during the movement of a two-phase systems in horizontal pipe. Izv. Vses. Teplotek. Inst. 1, 16–23.

Beatie, D.R.H., Whalley, P.B., 1982. A simple two-phase flow frictional pressure drop calculation method. Int. J. Multiphase Flow 8, 83–87.

Brackbill, J.U., Kothe, D.B., Zemach, C.A., 1992. A continuum method for modeling surface tension. J. Comput. Phys. 100, 335–354.

Brauner, N., Moalem-Maron, D., 1992. Identification of the range of small diameter conduits, regarding two-phase flow pattern transition. Int. Commun. Heat Mass Transfer 19, 29–39.

Chisholm, D., 1967. A theoretical basis for the Lockhart–Martinelli correlation for two-phase flow. Int. J. Heat Mass Transfer 10, 1767–1778.

Cicchitti, A., Lombardi, C., Silvesti, M., Solddaini, G., Zavalluilli, R., 1960. Two-phase experiments – Pressure drop, heat transfer and burnout measurement. Energy Nucl. 7, 407–425.

Dukker, A.E., Wicks III, M., Cleveland, R.G., 1964. Pressure drop and hold-up in two-phase flow. AIChE J. 10, 38–51.

Einstein, A., 1906. A new determination of the molecular dimensions. Ann. Phys. 19 (2), 289–306.

Ghidersa, B.E., Wörner, M., Cacuci, D.G., 2004. Numerical simulation of bubble-train flow with heat transfer in a square mini-channel. In: Proc. 5th Int. Conf. Multiphase Flow, Yokohama, Japan, May 30–June 4, 2004, Paper no. 567.

Himeno, T., Watanabe, T., Konno, A., 2005. Numerical analysis for propellant management in rocket tanks. J. Propul. Power 21, 76–86.

Irandoust, S., Andersson, B., 1989. Liquid film in Taylor flow through a capillary. Ind. Eng. Chem. Res. 28, 1684–1692.

Kandlikar, S.G., 2002. Fundamental issues related to flow boiling in minichannels and microchannels. Exp. Therm. Fluid Sci. 26, 389–407.

Kawahara, A., Chung, P.M.-Y., Kawaji, M., 2002. Investigation of two-phase flow pattern, void fraction and pressure drop in a microchannel. Int. J. Multiphase Flow 28, 1411–1435.

Kawahara, A., Sadatomi, M., Kumagae, K., 2006. Effects of gas–liquid inlet/mixing conditions on two-phase flow in microchannels. Progr. Multiphase Flow Res. I, 197–204.

Lee, J., Mudawar, I., 2005a. Two-phase flow in high-heat-flux micro-channel heat sink for refrigeration cooling applications: Part I – Pressure drop characteristics. Int. J. Heat Mass Transfer 48, 928–940.

Lee, J., Mudawar, I., 2005b. Two-phase flow in high-heat-flux micro-channel heat sink for refrigeration cooling applications: Part II – Heat transfer characteristics. Int. J. Heat Mass Transfer 48, 941–955.

Lin, S., Kwok, C.C.K., Li, R.Y., Chen, Z.H., Chen, Z.Y., 1991. Local frictional pressure drop during vaporization for R-12 through capillary tubes. Int. J. Multiphase Flow 17, 95–102.

Lockhart, R.W., Martinelli, R.C., 1949. Proposed correlation of data for isothermal two-phase two-component flow in pipes. Chem. Eng. Prog. 5, 39–48.

McAdams, W.H., 1954. Heat Transmission. third ed.. McGraw-Hill, New York.

Mishima, K., Hibiki, T., 1996. Some characteristics of air–water two-phase flow in small diameter vertical tubes. Int. J. Multiphase Flow 22, 703–723.

Monde, M., Mitsutake, Y., 1995. Enhancement of heat transfer due to bubbles passing through a narrow vertical rectangular channel (Change in heat transfer along flow). Heat Mass Transfer 31, 77–82.

Owens, W.L., 1961. Two-phase pressure gradient. Int. Dev. in Heat Transfer, Part II. ASME, New York.

Serizawa, A., 2006. Gas–liquid two-phase flow in microchannels. In: Crowe, C.T. (Ed.), Multiphase Flow Handbook. CRC Press (Chapter 11.1).

Serizawa, A., Feng, Z., Kawara, Z., 2002. Two-phase flow in a microchannels. Exp. Therm. Fluid Sci. 26, 703–714.

Sussman, M., Fatemi, E., 1999. An efficient interface-preserving level set redistancing algorithm and its application to interfacial incompressible flow. SIAM J. Sci. Comput. 20, 1165–1191.

Sussman, M., Smereka, P., Osher, S., 1994. A level set approach for computing solutions to incompressible two-phase flow. J. Comput. Phys. 114, 146–159.

Taylor, G.I., 1961. Deposition of a viscous fluid on the wall of a tube. J. Fluid Mech. 10, 161–165.

Thome, J.R., Dupont, V., Jacobi, A.M., 2004. Heat transfer model for evaporation in microchannels, Part I: Presentation of the model. Int. J. Heat Mass Transfer 47, 3375–3385.

Thulasidas, T.C., Abraham, M.A., Cerro, R.L., 1997. Flow patterns in liquid slugs during bubble-train flow inside capillaries. Chem. Eng. Sci. 52, 2947–2962.

Ua-arayaporn, P., 2005. Numerical simulation of gas–liquid two-phase convective heat transfer in a micro tube. M. Eng. Thesis, The University of Tokyo.

Wallis, G.B., 1969. One-Dimensional Two-Phase Flow. McGraw-Hill, New York.

Yabe, T., Aoki, T., Sakaguchi, G., Wang, P.Y., Ishikawa, T., 1991. The compact CIP (Cubic-Interpolated Pseudo-particle) method as a general hyperbolic solver. Comput. Fluids 19, 421–431.

Yabe, T., Xiao, F., Utsumi, T., 2001. The constrained interpolation profile method for multiphase analysis. J. Comput. Phys. 169, 556–593.